DRA

(NASA-CR-163704) OUTER PLANET INVESTIGATIONS USING A CCD CAMERA SYSTEM Final Report (Science Applications, Inc.) 26 p HC A03/MF A01 CSCL 14E

N81-11362

Unclas G3/35 16951

OUTER PLANET INVESTIGATIONS USING A CCD CAMERA SYSTEM

NASW-3332

FINAL REPORT

NOVEMBER 1980

Michael J. Price

Science Applications, Inc.
5055 E. Broadway, Suite A-214
Tucson, Arizona 85711
Tel: 602-748-7400

SAI PROJECT: 1-125-03-477-00

1.0 INTRODUCTION

Two-dimensional CCD (Charge Coupled Device) imaging systems provide the capabilities of high quantum efficiency, low background noise, and inherent spatial quantization of the image. In a unique industry/academia research and development effort, we proposed to use an existing SAI/EVC prototype CCD imaging system in collaboration with the staff of Lowell Observatory to obtain imaging data from a wide variety of planetary targets. We proposed to supplement our CCD observations with UBV photoelectric pinhole scan photometry to provide calibration of the system. Emphasis during our observational program was to be placed on Saturn, in view of the flybys by Pioneer 11 and the Voyager spacecraft. Our results are contained in this report.

2.0 CCD PROGRAM

Fabrication of the SAI/EVC Camera was successfully completed under the direction of Mr. Robert D. Smith on 1979 December 28 with funds supplied by SAI under Internal Research and Development Project 1-058-73-048-00. Major digital/analog functions of the system were demonstrated at the facility of the Electronic Vision Corporation in San Diego, California.

The CCD Camera was installed at Lowell Observatory on the 72-inch aperture Perkins telescope for initial operational tests during the period 1980 January 4-6. Digital interfaces in the camera and computer were brought on line together with the computer software. The data transmission link was verified. On 1980 January 7, the CCD Camera was shipped back to the Electronic Vision Corporation for use on another SAI project with Gulf General Atomic. System measurements were also to be made. In addition, efforts were to be made to reduce the analog noise to a level acceptable for very low light level photometry.

During the period 1980 February 15-20, the CCD Camera was again at Lowell Observatory. The analog noise problem was found to have been satisfactorily corrected by the Electronic Vision Corporation. When cooled with liquid air, the CCD chip produced minimum noise. During on-site laboratory testing, data transfer from the camera buffer to the storage computer was found to present a problem. Selection of the image region for storage was incorrect. The region stored did not correspond to the region selected. The problem was identified in the hardware. It was a circuit wiring problem. The CCD Camera (plus cold box) was shipped to the Electronic Vision Corporation (San Diego) so that the problem could be corrected.

On 1980 March 17, the CCD Camera was returned to Lowell Observatory. Laboratory tests carried out on March 20/21 showed that the hardware wiring problem had been corrected. The image region selected for storage was properly read out and stored within the computer. The CCD Camera was then mounted on the Perkins reflector. On 1980 April 4, experimental images were obtained of an individual star (apparent visual magnitude ≈ 2). Data were

taken through a narrow-band filter (200Å) at a wavelength of 8000Å. Within a single frame (1/60 sec. exposure), a few individual pixels were found to be saturated. Although the CCD sensitivity was high, multi-frame integrations were required to reach the planetary targets of interest viz., Saturn, Uranus, Neptune, and their satellites. It was found that multi-frame imaging could not be obtained. The problem appeared to lie in the hardware wiring. The instrument was therefore shipped back to San Diego for further electronic work.

Shortly thereafter the project received a severe setback in the accidental death of the EVC technician assigned to the CCD system. She was killed in an automobile accident late one night on her way home from the laboratory. She had been working overtime in an effort to get the system working correctly while the planetary objects of interest remained accessible to observation.

During 1980 May, EVC found the hardware wiring problem. The instrument was rewired and shipped back to Lowell Observatory. During 1980 June, laboratory tests in Flagstaff showed that the integration problem had been solved.

During 1980 July, observational tests on the Perkins telescope showed that the CCD Camera had suffered a major loss of sensitivity by a factor ~10,000. Consultation with the Electronic Vision Corporation identified the problem. Certain voltages within the electronics package had been incorrectly set. With the proper settings, laboratory tests showed that the sensitivity was much improved. On-site adjustment of the CCD system was seriously affected by the unforeseen resignation of the only electronic technician at Lowell Observatory.

Further observational tests were carried out on the Perkins telescope during 1980 August. Vega was imaged in both wide- and narrow-wavebands. Although the system integrated satisfactorily, hardcopy data-readout could not be achieved. Images could be viewed on a CRT display however. Although the sensitivity of the system had improved by a factor of 100 compared with the July observations, the effective quantum efficiency remained no greater than 1 percent. In addition, the output from the CCD chip had become rather

noisy. It is unclear whether the lack of sensitivity is caused by a poor CCD chip or by the system electronics package. Since the planetary targets of interest were rapidly becoming inaccessible, work with the CCD Camera was indefinitely suspended.

3.0 PHOTOELECTRIC AREA SCANNING PHOTOMETRY

The Franz area-scanner was used to obtain photometric calibration data for the Saturn disk. On the night of opposition in 1980 March, UBV pinhole scans of the planet were made parallel to the equator. Ten latitudes were scanned, covering the entire disk from the north to the south polar regions. UBV scans were also made along the central meridian of the planet from the north to the south pole. Seeing was excellent, and reliable point spread function data were obtained in each color. Photometric calibration was provided by a UBV standard star.

The equatorial and polar scans were used to investigate the structure of the Saturn atmosphere. The observational geometry was optimum. Not only was Saturn at opposition, but the ring system was essentially edge-on to both the Sun and Earth. The analysis indicates that the atmosphere of Saturn can be represented by a finite clear H_2 layer overlying a semi-infinite absorbent aerosol haze. The extent of the clear H_2 region appears to be latitude-dependent. The H_2 column-density varies systematically from $\sim$15 km amagat over the equatorial and polar regions to $\sim$31 km amagat at temperate latitudes. The hemispheres of the planet are similar, but not identical. An earlier conclusion, that the aerosol haze is strongly absorbent in the ultraviolet, is confirmed; its effective U-band single scattering albedo is $\sim$0.4. Latitudinal disk structure at visual wavelengths appears to be the result of local variations in the volume density of absorbent particles in the aerosol layer. A paper reporting the results has been submitted for publication. A preprint is reproduced in the Appendix.

4.0 PUBLICATIONS

During the present contract, two papers were accepted and published, by ICARUS. The titles are:

"Neptune: Limb Brightening Within the 7300 Angstrom Methane Band" (with O.G. Franz), Icarus 41, 430, 1980.

"Neptune's Rotation Period: A Correction and a Speculation on the Difference Between Photometric and Spectroscopic Results" (with M.J.S. Belton, L. Wallace, and S.M. Hayes), Icarus 42, 71, 1980.

In addition, a paper entitled "Saturn: New UBV Photoelectric Pinhole Scans of the Disk", was presented at the 12th Annual Meeting of the Division for Planetary Sciences of the American Astronomical Society, 1980 October 14-17.

APPENDIX

SATURN: UBV PHOTOELECTRIC PINHOLE SCANS OF THE DISK. II

MANUSCRIPT SUBMITTED TO ICARUS
FOR PUBLICATION

SATURN: UBV PHOTOELECTRIC PINHOLE SCANS OF THE DISK.II.

Michael J. Price[†]
Science Applications, Inc.
5055 E. Broadway, Suite A-214
Tucson, Arizona 85711

and

Otto G. Franz
Lowell Observatory
P. O. Box 1269
Flagstaff, Arizona 86002

[†]Adjunct Scientist, Lowell Observatory

No. of Copies: 4

No. of MS Pages: 19

No. of Figures: 6

No. of Tables: 0

Person to whom proofs should be sent:

Dr. Michael J. Price
Science Applications, Inc.
5055 E. Broadway, Suite A-214
Tucson, Arizona 85711

Proposed running head:

SATURN DISK PHOTOMETRY

ABSTRACT

During the 1980 Saturn apparition, calibrated UBV pinhole scans of the disk were obtained with a photoelectric area-scanning photometer. Point spread function data were also taken. Equatorial and polar scans were used to investigate the structure of the Saturn atmosphere. The observational geometry was optimum. Not only was Saturn at opposition, but the ring system was essentially edge-on to both the Sun and Earth. Our analysis indicates that the atmosphere of Saturn can be represented by a finite clear H_2 layer overlying a semi-infinite absorbent aerosol haze. The extent of the clear H_2 region appears to be latitude-dependent. The H_2 column-density varies systematically from ~15 km amagat over the equatorial and polar regions to ~31 km amagat at temperate latitudes. The hemispheres of the planet are similar. Our earlier conclusion, that the aerosol haze is strongly absorbent in the ultraviolet, is confirmed; its effective U-band single scattering albedo is ~0.4 Latitudinal disk structure at visual wavelengths appears to be the result of local variations in the volume density of absorbent particles in the aerosol layer.

INTRODUCTION

In Paper I, Franz and Price (1979) reported UBV pinhole scans of the Saturn disk made with a photoelectric area-scanning photometer. Limb profiles, spaced parallel to the equator, were obtained over the entire southern hemisphere of the planet. Saturn was found to exhibit strong limb-brightening in the ultraviolet, moderate limb-brightening at blue wavelengths, and strong limb-darkening in the visual region of the spectrum. Latitudinal variations were found. In general, the degree of limb-brightening decreased towards the polar region. Pronounced asymmetry was frequently apparent in the disk profiles in each color; the sunward limb was significantly brighter than the opposite limb. This asymmetry depended on phase angle. Approaching zero at opposition, it reached a maximum near quadrature. The observations were interpreted on the basis of an elementary radiative transfer model. The Saturn atmosphere was approximated by a finite homogeneous layer of isotropically scattering particles overlying a Lambert scattering haze or cloud layer. The reflectivity of the aerosol region was a strongly dependent function of wavelength. The Lambert scattering layer was found to absorb strongly in the ultraviolet region of the spectrum. The best-fitting model consisted of a clear H_2 layer of column density ~31 km amagat above the haze or clouds; the maximum permitted H_2 column density was 46 km. amagat. The H_2 column density above the equatorial region appeared to be less than at temperate latitudes. The phase dependent asymmetry of the disk profiles was found to be a natural consequence of the scattering geometry.

Four deficiencies are present in Paper I. First, no photometric standard stars were observed. Consequently, the Saturn disk photometry could not be placed on the standard UBV system; it remained uncalibrated. So comparison of theory with observation was necessarily qualitative only. Second, the point spread function in each color was unknown. Theoretical predictions could not be smeared to permit proper comparison with the observational data. Third, the observational geometry left much to be desired. Tilt of the rings with respect to the line-of-sight prevented observation of much of the northern hemisphere

of the planet. Furthermore, light scattered from the ring system contaminated the disk scans, particularly at the limb of the planet. Fourth, the radiative transfer model was too elementary. Adopting a Lambert scattering surface for the visible haze or cloud layer was simplistic. During the 1979/80 Saturn apparition, the ring system was essentially edge-on to both the Sun and Earth, providing an excellent opportunity to obtain reliable photometry of the disk. Each deficiency in the earlier work was corrected.

OBSERVATIONS

On 1980 March 14, UBV photoelectric photometry of the Saturn disk was carried out with the area-scanner described by Franz (1970) mounted on the 1.8 meter aperture Perkins telescope. The scanning aperture was a 100 μm (0.645 arc. sec) pinhole, and the effective scan length was 30 arc. sec. Samples were taken at an interval of 0.0778 arc. sec. Multi-color scans, spread over both hemispheres of the planet, were taken along ten chords spaced parallel to the major axis of the ring system. In addition, a multi-color polar scan was obtained along the central meridian of the planet. The nominal scan locations, accurate to better than one pinhole diameter, are shown superimposed on the Saturn disk in Fig. 1. Taken from the 1980 American Ephemeris and Nautical Almanac, the relevant polar and equatorial diameters are 17.65 arc. sec and 19.73 arc. sec, respectively. UBV stellar slit scan data were also obtained to calibrate the point spread function. The slit width was 100 μm (0.645 arc. sec); the slit length was 2mm (12.9 arc. sec). Scans were made of an individual star, of apparent visual magnitude ~8, near the planet.

For Saturn, photometric noise was held to a minimum by using a compositing technique for each color and scan location. Each composite profile was obtained by summing three individual scans matched according to their photometric centroids. Each U-scan was obtained by integrating 20 one-second sweeps; each B- or V-scan resulted from the integration of 5 one-second sweeps only. For the star, each composite was obtained by summing a pair of individual scans in each color. Each individual scan was obtained by integrating 20 one-second sweeps.

By good fortune, the observations were carried out during the night of opposition, when the ring system was almost precisely edge-on to both the Earth and Sun. Specifically, the phase angle was 0.25 degrees only, while the Saturnicentric declinations of the Earth and Sun were -0.050 degrees and +0.167 degrees, respectively. These circumstances greatly simplified the observational geometry. Each scan location parallel to the major axis of the ring system referred to a unique latitude on the planet; the polar scan referred to a unique longitude.

Contamination of the Saturn disk photometry by light from the ring system was insignificant. With the Earth and Sun close to but on opposite sides of the ring plane, the surface brightness of the system was extremely low. Furthermore, the projected area of the rings was negligible; the minor axis of the system was only 0.04 arc. sec. The rings were detectable in the equatorial scan only, and then barely above the sky background itself. Their effect was easily and accurately removed.

Absolute calibration of the Saturn disk photometry was needed to permit a physical interpretation by means of theoretical atmospheric scattering models. Specifically, the measured photoelectron counts within each disk profile must be related to the radiative transfer quotient I/F, where I denotes the specific intensity at the appropriate location on the disk of the planet; the solar flux at Saturn within the relevant waveband is πF. By integrating the total photon counts over the entire image of Saturn, we can obtain a calibration based on the geometrical albedo of the planet.

Extremities of the Saturn image were determined from an examination of the polar and equatorial profiles of the disk. Since all ten constant latitude profiles showed remarkable symmetry about the central meridian, they were aligned in longitude by matching the locations of their photometric centroids. Two-dimensional integration was then carried out over the entire image of Saturn. Linear interpolation in latitude between adjacent profiles was used. Our estimated uncertainty in the total photoelectron count inferred for the planet was $\pm$ 3 percent.

UBV geometrical albedos for the disk of Saturn have been published by Irvine and Lane (1971). Their values were derived for the situation of zero phase angle. Specifically, they obtained p_U equal 0.166; p_B equal 0.297; and p_V equal 0.429. In the absence of temporal effects, their results would be directly relevant to our analysis. Standard UBV photoelectric photometry was therefore carried out to determine whether the reflectivity of the disk had changed significantly during the last decade. Slit-scan observations were obtained on 1980 July 4; calibration was provided by two standard stars. Saturn was beyond quadrature; its phase angle was 5.77 degrees. Since the ring system remained essentially edge-on to both the Earth and Sun, its contribution to the apparent brightness of the planet was

negligible. The inferred geometrical albedos were: p_U equal 0.191; p_B equal 0.271; and p_V equal 0.411. In view of the lack of knowledge of the phase effect, no attempt was made to correct the results to zero phase angle. Each geometrical albedo was estimated to be uncertain by ± 5 percent. Comparison with Irvine and Lane (1971) suggests that no significant changes have occurred in the UBV reflectivities of the disk. For our analysis, therefore, we adopted the geometrical albedos given by Irvine and Lane (1971).

Atmospheric turbulence, together with diffuse instrumental scatter, is responsible for the observed point spread function. In earlier investigations of Uranus, we showed that the point spread function is well represented by the summation of two colocated but distinct Gaussian curves. Normalizing the point spread function, f(r), to unit total energy, we can write its radial distribution in the general form

$$f(r) = \frac{1}{\pi\left[A\sigma_1^2 + B\sigma_2^2\right]} \left\{A \exp\left[-r^2/\sigma_1^2\right] + B \exp\left[-r^2/\sigma_2^2\right]\right\} \qquad (1)$$

where A, B, σ_1 and σ_2 are constants. Optimum sets of PSF parameters for each waveband were obtained from the composite stellar slit scans by the method described by Price and Franz (1979). Within the U-band, we found A = 1; B = 0.0382; σ_1 = 0.812 arc. sec; and σ_2 = 2.131 arc. sec. Within the B-band, we found A = 1; B = 0.0914; σ_1 = 0.713 arc. sec; and σ_2 = 1.744 arc. sec. Within the V-band, we found A = 1; B = 0.1604; σ_1 = 0.613 arc. sec; and σ_2 = 1.285 arc. sec. Notice that the point spread function becomes narrower with increasing wavelength. For Flagstaff, the seeing was unusually good. Our best-fitting analytical stellar scans are compared with the observational data for each color in Fig. 2. Scaled with respect to each central intensity, the root mean square deviations between calculation and observation are 0.51, 0.60, and 0.60 percent for the U-, B-, and V-colors respectively.

ANALYSIS

Convolution of Saturn's intensity distribution with both the pinhole aperture and the atmospheric spread function is discussed in the Appendix. For convenience, we selected the polar and equatorial scan data for detailed interpretation. But, first, we chose to remove the smearing introduced by the finite diameter of the pinhole. We used the Bayesian rectification technique developed by Lucy (1974). High frequency photometric noise was automatically removed by this rectification method. Theoretical intensity profiles, convolved with the line spread function, could then be compared directly with the rectified measurements.

Selection of a theoretical model for the Saturn atmosphere was based on the investigation reported in Paper I. We adopted the simplest plausible model. The Saturn atmosphere was assumed to consist of a clear H_2 layer of arbitrary optical thickness overlying a semi-infinite aerosol haze of arbitrary single scattering albedo. The H_2 molecules were assumed to scatter conservatively. In addition, an isotropic scattering phase function was adopted throughout. The corresponding radiative transfer problem has been solved by Sobolev (1974). His analytical solution may be used to compute the diffuse reflection properties of the planet. On the basis of the known observational geometry, we can safely equate the angles of incidence and emergence everywhere on the disk. To make the relevant computations, Saturn was assumed to have the figure of an oblate spheriod. The polar and equatorial diameters of the disk have already been listed.

Our initial selections of the radiative transfer parameters of the atmospheric model were based on the calibrated measurements of intensity at the center of the disk (I_0/F). In each color, the equatorial scan was found to be symmetrical; its photometric centroid therefore corresponded to the disk center. Our data give I_0/F values equal to 0.116, 0.323, and 0.531 for the U, B, and V colors, respectively. Using the Sobolev (1974) method, we computed I_0/F as a function both of the optical thickness (τ) of the clear H_2 layer and of the single scattering albedo ($\tilde{\omega}$) of the underlying aerosol haze. Our principal results are illustrated in Fig. 3. For comparison, the measured I_0/F values are also shown. In the U-band, the

optical thickness of the clear H_2 region cannot be greater than 0.5, while the single scattering albedo of the aerosol haze must be less than 0.55. In the B-band, we require $\tilde{\omega} < 0.875$; in the V-band, $\tilde{\omega} < 0.975$. In our model atmosphere, Rayleigh scattering from the H_2 molecules is responsible for the opacity of the clear upper layer. Using relevant data from Ford and Browne (1973), we can readily show that the individual U(λ3750 Å), B(λ4450 Å) and V(λ5500 Å) optical thicknesses are in the respective proportions 1:0.5:0.2. For the B-band, therefore, we require $\tau < 0.25$; in the V-band, $\tau < 0.1$.

If Saturn is assumed to be rotationally symmetric, its atmospheric parameters will be uniquely defined at each latitude. We can therefore use the equatorial scans of the planet to further refine our choices both for the optical thickness of the clear H_2 layer and for the single scattering albedo of the underlying aerosol haze. Only certain combinations of parameters are permitted by our original constraint upon the central intensity of the disk. Our optimum results for the U-band are illustrated in Fig. 4. For τ equal to 0.2 with $\tilde{\omega}$ equal to 0.4, the fit between theory and observation is extremely good. In fact, two other permitted combinations of parameters (viz., $\tilde{\omega} = 0.3$, $\tau = 0.3$ and $\tilde{\omega} = 0.5$, $\tau = 0.1$) are quite unsatisfactory. A U-band optical thickness of 0.2 is equivalent to an H_2 column-density of 15.4 km. amagat. Setting the B-band optical thickness to be 0.1, we can readily determine the corresponding optimum choice for the single scattering albedo of the aerosol haze. Our results are also shown in Fig. 4. For the B-band, we obtain $\tilde{\omega}$ approximately equal to 0.85. For the V-band, the effect of the clear H_2 layer is insignificant; the relevant optical thickness is too small. Computed V-band equatorial scans of the planet are shown in Fig. 4. With τ equal to zero, we find $0.95 < \tilde{\omega} < 0.975$.

Our polar scans of Saturn can be used to investigate latitudinal variations in its atmospheric structure. In the ultraviolet, the diffuse reflectivity of the planet is determined principally by scattering within the clear H_2 layer because the underlying aerosol haze is so strongly absorbent. Lack of detailed belt/band structure in the U-band data suggests the adoption of a unique value for the single scattering albedo of the aerosol layer. Variations in the surface brightness with latitude

can then be explained by changes in the optical thickness of the clear H_2 layer. By contrast, at visual wavelengths, scattering within the aerosol layer determines the surface brightness of the planet; the relevant optical thickness of the clear H_2 layer is insignificant. Belt/band structure present in the V-band data can be explained by latitudinal variations in the effective single scattering albedo of the aerosol haze.

Our U-band polar scan of Saturn is compared with theory in Fig. 5. While the single scattering albedo of the aerosol haze ($\tilde{\omega}$) was held constant at the equatorial value (0.4), the optical thickness of the clear H_2 layer was varied through the range $0 \leq \tau \leq 0.5$. Our results show that τ varies continuously with latitude, passing through a maximum value ~ 0.4 at temperate latitudes. Its behavior with respect to the equator is not quite symmetrical; minor differences between the hemispheres are apparent. Within the polar regions, the optical thickness of the clear H_2 layer appears to be in the range 0.1 - 0.2. Over the equator, we find $\tau \sim 0.2$.

Our B-band polar scan of Saturn is also compared with theory in Fig. 5. While the relevant optical thickness of the clear H_2 layer was held constant at the equatorial value, the single scattering albedo of the underlying aerosol haze was varied throughout the range $0.8 \leq \tilde{\omega} \leq 0.9$. Small local variations in $\tilde{\omega}$ easily explain latitudinal structure in the observational data. That conclusion also holds for the V-band. Observation and theory are compared in Fig. 5. While ignoring the clear H_2 layer, we varied the single scattering albedo of the aerosol haze through the range $0.925 \leq \tilde{\omega} \leq 0.975$.

For comparison, Fig. 6 shows ultraviolet, blue, and green images of Saturn obtained at Mauna Kea on 1980 March 13 by the International Planetary Patrol Program. Each image is a composite of seven individual exposures. The three composites were made with identical materials, contrast, maximum density, and image scale. Note that the green image is strongly limb-darkened and smaller than the limb-brightened ultraviolet image. In the blue, the Saturn disk appears of more nearly uniform brightness. Belt/band structure is readily apparent in the blue and green images but not in the ultraviolet.

SUMMARY

Current models of the Saturn atmosphere were reviewed in Paper I. Present opinion holds that a clear region of H_2 column-density in the range 7-37 km. amagat overlies an absorbent aerosol haze; absorption is strongest in the ultraviolet. Our analysis supports earlier suggestions that the extent of the clear region is latitude-dependent. The H_2 column-density varies systematically from $\sim$ 15 km. amagat over the equatorial and polar regions to $\sim$ 31 km. amagat, at temperate latitudes. Both hemispheres are similar. We confirm that the underlying aerosol haze is strongly absorbent in the ultraviolet; its effective U-band single scattering albedo is $\sim$ 0.4. Finally, we interpret latitudinal belt/band structure at visual wavelengths to be the result of local fluctuations in the volume density of the absorbing particles in the aerosol layer.

APPENDIX

Define the Saturn disk center to be the origin of x,y cartesian co-ordinate axes. For convenience, suppose the x-axis is parallel to the equator while the y-axis is along the central meridian of the planet. Further, write the specific intensity of the unsmeared Saturn disk $g(x,y)$; the intensity within the Saturn image $i(x,y)$; the point spread function $s(x,y)$; and the pinhole broadening function $p(x,y)$. By definition, we can write

$$i(x,y) = \iint I(u,v) \exp\left\{2\pi j(ux + vy)\right\} \, dudv \qquad (A.1)$$

where $I(u,v)$ is the Fourier transform of the Saturn image at spatial frequencies u,v in the equivalent cartesian co-ordinate system. Making use of the Fourier transform convolution theorem, we can write

$$I(u,v) = G(u,v)\, P(u,v)\, S(u,v) \qquad (A.2)$$

where capitalization of each function denotes the corresponding Fourier transform.

Inspection of the Saturn image shows that the intensity exhibits separable behavior in each variable in the vicinity of each co-ordinate axis. Normal to each axis, the intensity is essentially constant over a span equivalent to the smear produced by the convolution of the pinhole aperture with the point spread function. In which case, we can write

$$g(x,y) = g_1(x) \cdot g_2(y) \qquad (A.3)$$

where

$$g_1(x) = 1 \quad \text{as} \quad x \to 0 \qquad (A.4)$$

and

$$g_2(y) = 1 \quad \text{as} \quad y \to 0 \tag{A.5}$$

Taking the Fourier transform of both sides of (A.3), we have

$$G(u,v) = G_1(u)\, G_2(v) \tag{A.6}$$

in the usual notation. Making use of the Dirac δ-function, we can write

$$G_1(u) = \delta(u) \tag{A.7}$$

for a polar scan, and

$$G_2(v) = \delta(v) \tag{A.8}$$

for an equatorial scan.

Considering the equatorial scan ($y = 0$) in greater detail, we can rewrite (A.2) in the form

$$I(u,v) = G_1(u)\, \delta(v)\, P(u,v)\, S(u,v). \tag{A.9}$$

Substituting (A.9) into (A.1), we have

$$i(x,o) = \iint G_1(u)\, \delta(v)\, P(u,v)\, S(u,v) \exp\,[-2\pi jux]\; dudv \tag{A.10}$$

which reduces to

$$i(x,o) = \int G_1(u)\, P(u,o)\, S(u,o) \exp\,[-2\pi jux]\; du. \tag{A.11}$$

By definition, we have

$$P(u,o) = \iint p(x,y) \exp [-2\pi jux] \, dxdy \tag{A.12}$$

or

$$P(u,o) = \int \ell_p(x) \exp [-2\pi jux] \, dx \tag{A.13}$$

where

$$\ell_p(x) = \int p(x,y)dy = \frac{2}{\pi}\sqrt{1 - (x/\xi)^2} \tag{A.14}$$

where ξ is the pinhole radius. Similarly, we have

$$S(u,o) = \iint s(x,y) \exp [- 2\pi jux] \, dxdy \tag{A.15}$$

or

$$S(u,o) = \int \ell_s(x) \exp [- 2\pi jux] \, dx \tag{A.16}$$

where

$$\ell_s(x) = \int s(x,y)dy \tag{A.17}$$

But s(x,y) is a separable function since

$$s(r) = \frac{1}{\pi\left[A\sigma_1^2 + B\sigma_2^2\right]} \left\{A \exp\left[-r^2/\sigma_1^2\right] + B \exp\left[-r^2/\sigma_2^2\right]\right\} \quad (A.18)$$

where

$$r^2 = x^2 + y^2 \quad (A.19)$$

and A, B, σ_1 and σ_2 are constants. It can be easily shown that

$$\ell_s(x) = \frac{1}{\sqrt{\pi}\left[A\sigma_1^2 + B\sigma_2^2\right]} \left\{A\sigma_1 \cdot \exp\left[-x^2/\sigma_1^2\right] + B\sigma_2 \cdot \exp\left[-x^2/\sigma_2^2\right]\right\} \quad (A.20)$$

The polar scan can be treated in a similar manner. Each convolution may be carried out using the Fast Fourier Transform algorithm developed by Cooley and Tukey (1965).

ACKNOWLEDGMENTS

We thank S.E. Jones for producing the composite images of Saturn from International Planetary Patrol photographs. This research was supported by the National Aeronautics and Space Administration under contract NASW-3332 and grant NGR-03-003-001. The equipment used to gather the photometric data was developed, assembled, and tested with the support of National Science Foundation grants GP-6983 and GP-20090.

REFERENCES

Cooley, J.W. and Tukey, J.W. (1965) "An Algorithm for the Machine Calculation of Complex Fourier Series", Math. Comp. 19, 297-301.

Ford, A.L. and Browne, J.C. (1973) "Rayleigh and Raman Cross-Sections For The Hydrogen Molecule", Atomic Data 5, 305-313.

Franz, O.G. (1970) "A Photoelectric Area Scanner for Astrometry and Photometry of Visual Double Stars", Lowell Obs. Bull. 7, 191-197.

Franz, O.G. and Price, M.J. (1979) "Saturn: UBV Photoelectric Pinhole Scans of the Disk", Icarus 37, 272-281.

Irvine, W.M. and Lane, A.P. (1971) "Monochromatic Albedos for the Disk of Saturn", Icarus 15, 18-26.

Lucy, L.B.(1974) "An Iterative Technique for the Rectification of Observed Distributions", Astron. J. 79, 745-754.

Price, M.J. and Franz, O.G. (1979) "Uranus: Narrow-Waveband Disk Profiles in the Spectral Region 6000 to 8500 Angstrums", Icarus 38, 267-287.

Sobolev, V.V. (1974) "Light Scattering in an Inhomogeneous Atmosphere", Astron. Zh. 51, 50-55.

FIGURE CAPTIONS

Fig. 1. Opposition measurements of the Saturn disk. The nominal pinhole scan positions are illustrated. The pinhole diameter was 0.645 arc. sec.

Fig. 2. UBV stellar slit scans: comparison of calculation with observation. Composite observational data are illustrated by the individual dots. The best-fitting analytical profiles are represented by the solid curves. The slit width was 0.645 arc. sec. The sample interval was 0.078 arc. sec.

Fig. 3. Diffuse reflection from the center of the Saturn disk. Theoretical I_0/F values are plotted versus the single scattering albedo ($\tilde{\omega}$) of the deep aerosol layer for extreme choices of the optical thickness (τ) of the overlying clear H_2 region. I_0 denotes the specific intensity of the disk center; the solar flux at Saturn is πF. UBV measurements of I_0/F are also shown.

Fig. 4. UBV Equatorial scans of the Saturn disk: comparison of theory with observation. Theoretical I/F predictions are illustrated by the solid curves. Relevant observational data are illustrated by the broken curves. Pinhole smearing has been removed from the observational data. I denotes the specific intensity; the solar flux at Saturn is πF. East is on the left. In view of the symmetry in the observational data, the photometric centroids were taken to be at the center of the disk.

Fig. 5. UBV Polar Scans of the Saturn disk: comparison of theory with observation. Theoretical I/F predictions are illustrated by the solid curves. Relevant observation data are illustrated by the broken curves. Pinhole smearing has been removed from the observational data. I denotes the specific intensity; the solar flux at Saturn is πF. South is on the left. For the observational data, the position of the disk center was inferred by matching the extremities of the scan with predictions from theory. Locating the disk center according to the specific intensity obtained from the equatorial scan was less precise. It served as a useful check however.

Fig. 6. International Planetary Patrol photographs of Saturn taken on 1980 March 13. Composite images in the ultraviolet, blue, and green are shown.

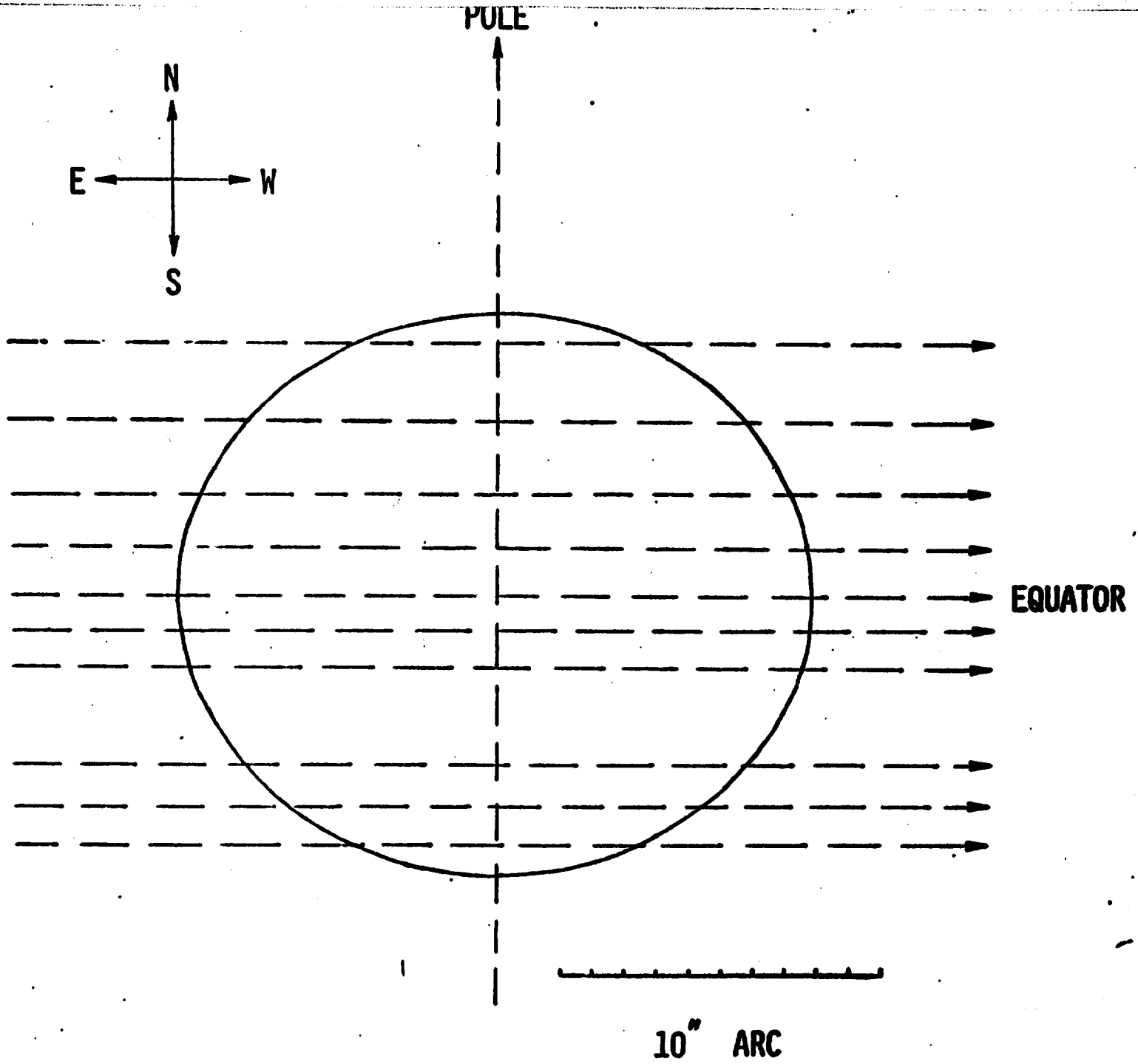

Fig. 1

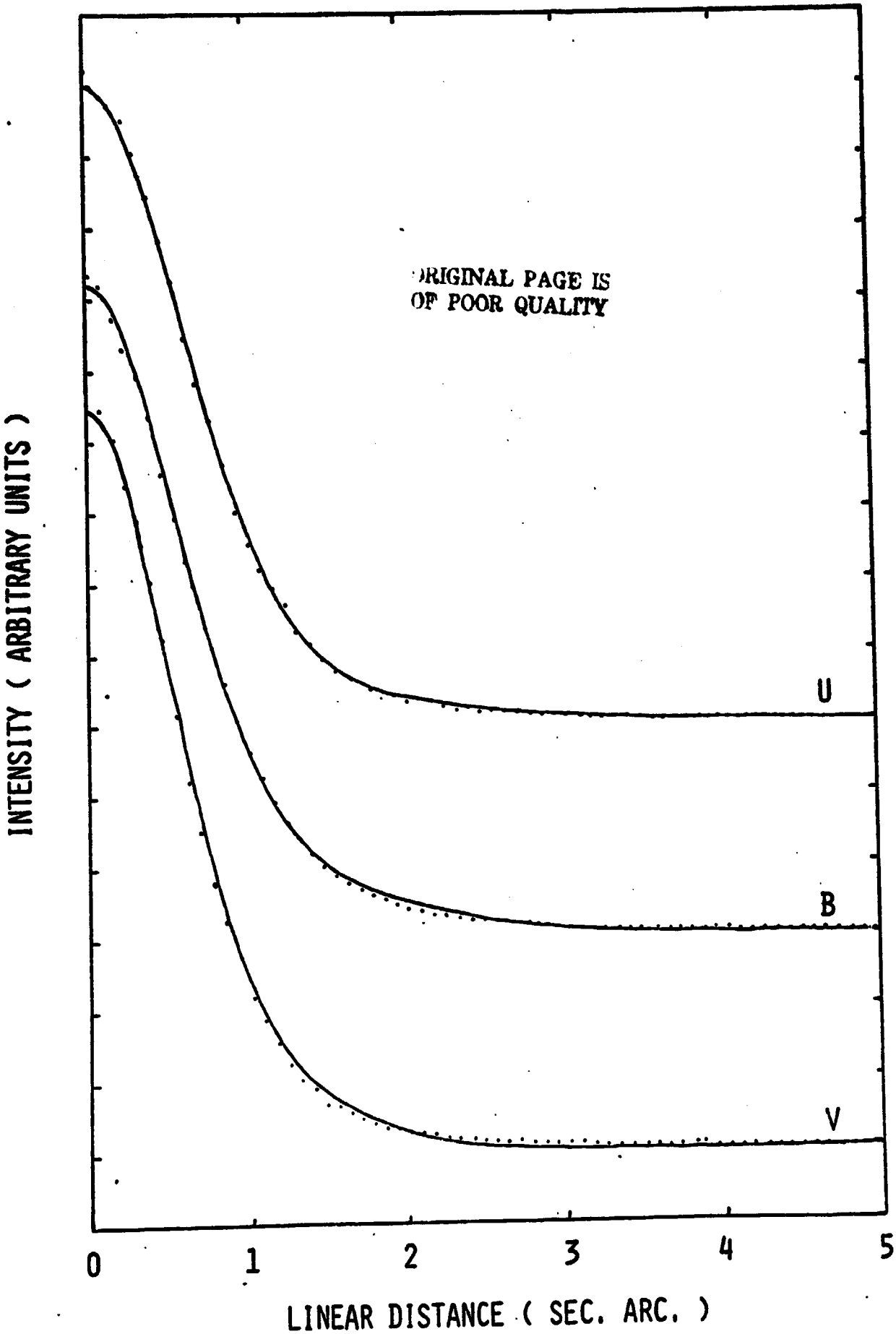
ORIGINAL PAGE IS
OF POOR QUALITY
INTENSITY (ARBITRARY UNITS)
U
B
V
0
1
2
3
4
5
LINEAR DISTANCE (SEC. ARC.)

Fig. 2

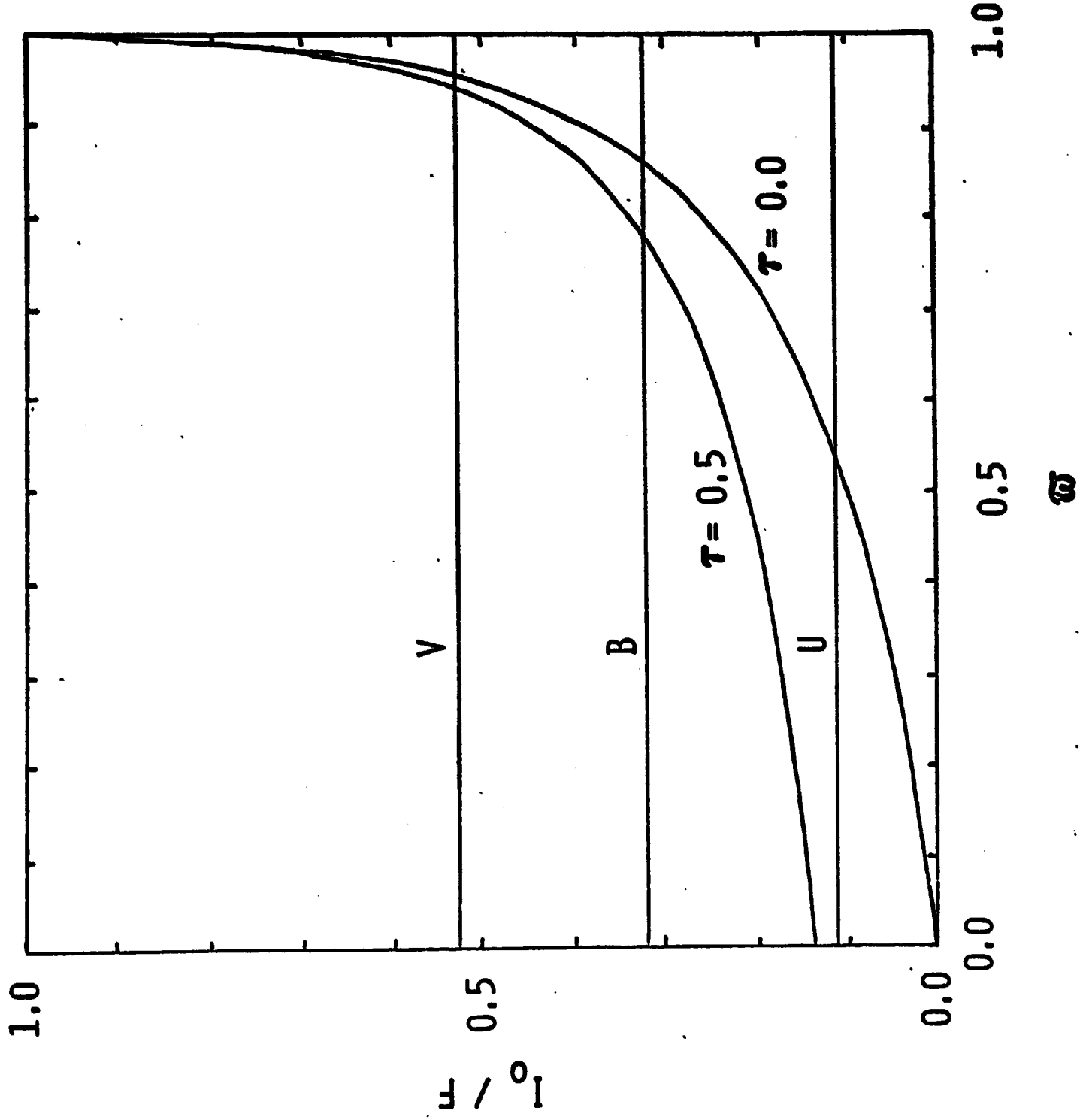

Fig. 3

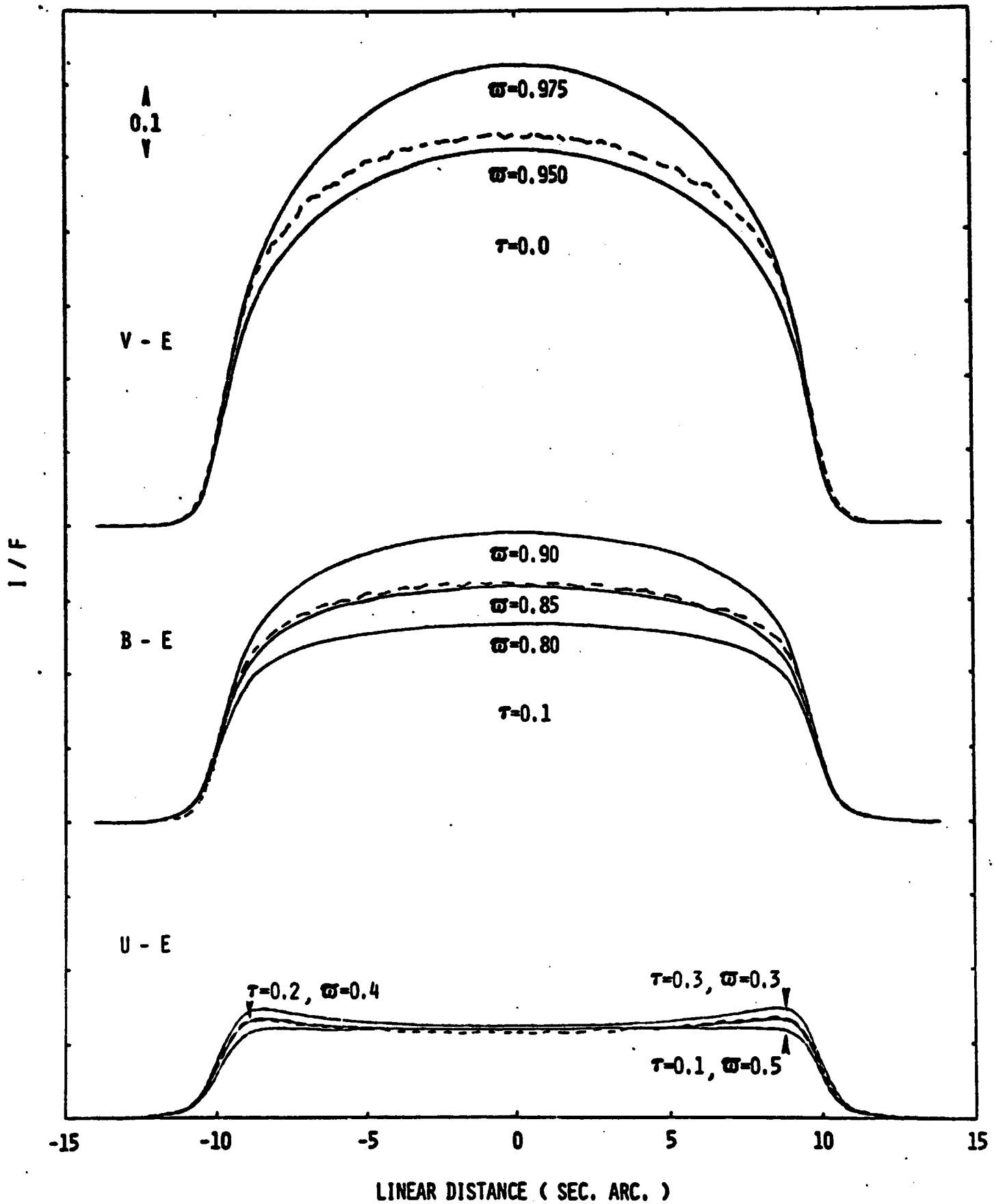
0.1
ϖ=0.975
ϖ=0.950
τ=0.0
V - E
ϖ=0.90
ϖ=0.85
ϖ=0.80
τ=0.1
B - E
U - E
τ=0.2, ϖ=0.4
τ=0.3, ϖ=0.3
τ=0.1, ϖ=0.5
I / F
-15
-10
-5
0
5
10
15
LINEAR DISTANCE (SEC. ARC.)

Fig. 4

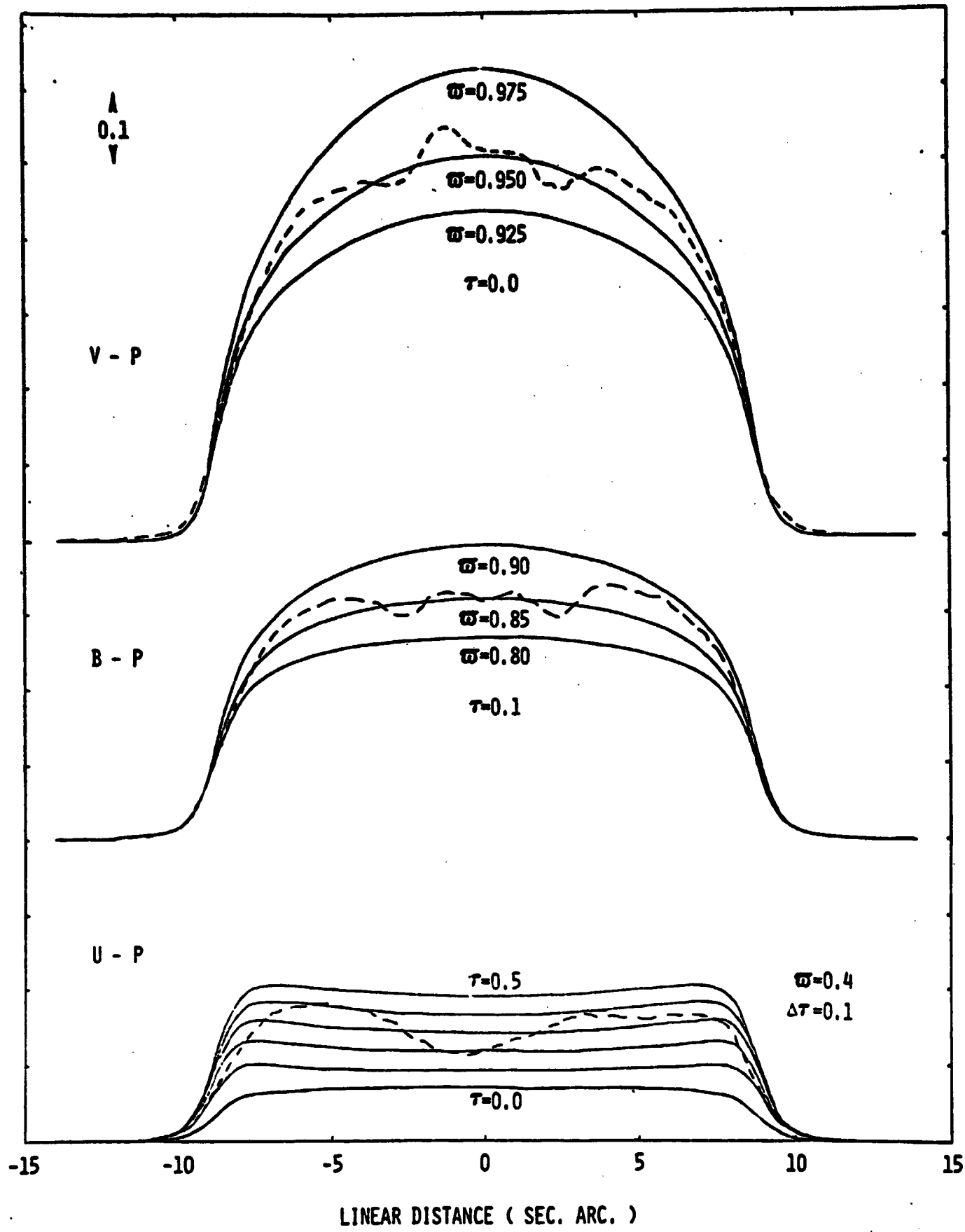
0.1
ϖ=0.975
ϖ=0.950
ϖ=0.925
τ=0.0
V - P
I / F
ϖ=0.90
ϖ=0.85
ϖ=0.80
τ=0.1
B - P
U - P
τ=0.5
ϖ=0.4
Δτ=0.1
τ=0.0
-15
-10
-5
0
5
10
15
LINEAR DISTANCE (SEC. ARC.)

Fig. 5

NORTH

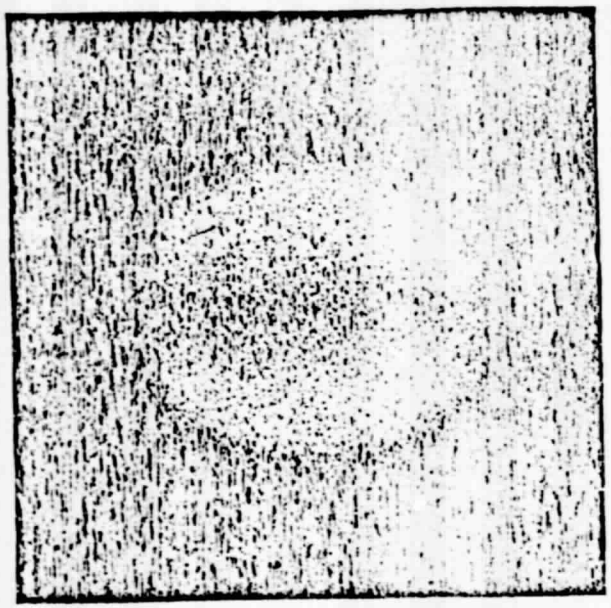

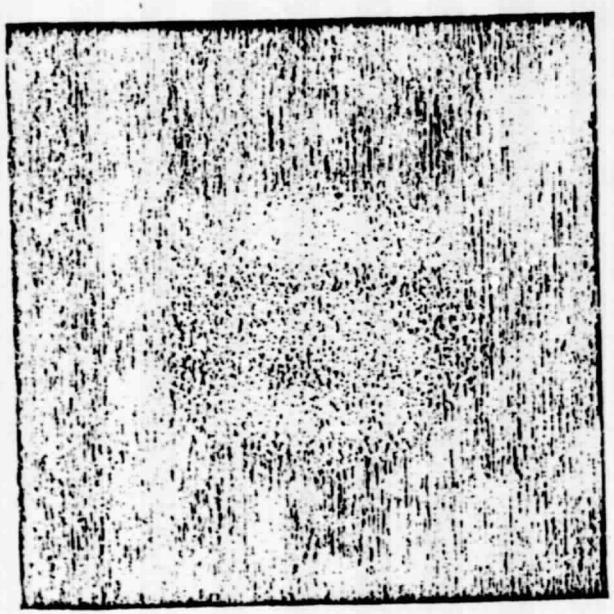

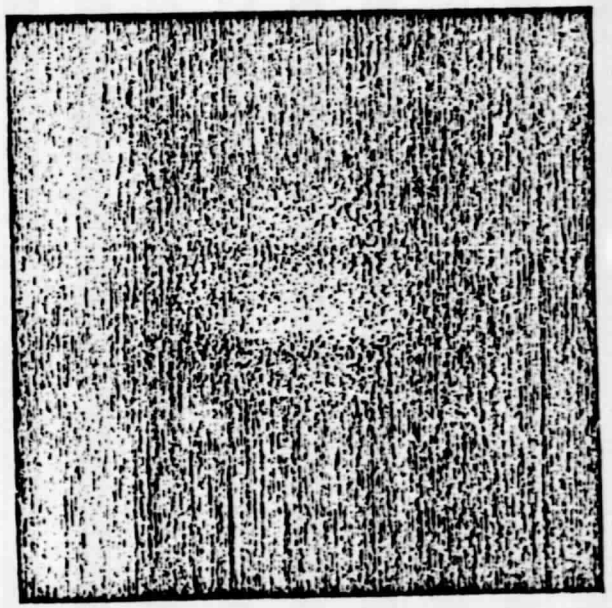

ULTRAVIOLET

BLUE

GREEN

Fig. 6